



This is a repository copy of *CFD–DEM modelling of particle entrainment in wheel–rail interface: a parametric study on particle characteristics*.

White Rose Research Online URL for this paper:

<https://eprints.whiterose.ac.uk/222578/>

Version: Published Version

Article:

Maramizonouz, S., Nadimi, S. orcid.org/0000-0002-0971-7089, Skipper, W. orcid.org/0000-0001-8315-2656 et al. (1 more author) (2025) CFD–DEM modelling of particle entrainment in wheel–rail interface: a parametric study on particle characteristics. *Railway Engineering Science*. ISSN 2662-4745

<https://doi.org/10.1007/s40534-024-00365-1>

Reuse

This article is distributed under the terms of the Creative Commons Attribution (CC BY) licence. This licence allows you to distribute, remix, tweak, and build upon the work, even commercially, as long as you credit the authors for the original work. More information and the full terms of the licence here:

<https://creativecommons.org/licenses/>

Takedown

If you consider content in White Rose Research Online to be in breach of UK law, please notify us by emailing eprints@whiterose.ac.uk including the URL of the record and the reason for the withdrawal request.



eprints@whiterose.ac.uk
<https://eprints.whiterose.ac.uk/>



CFD–DEM modelling of particle entrainment in wheel–rail interface: a parametric study on particle characteristics

Sadaf Maramizonouz¹ · Sadegh Nadimi¹ · William Skipper² · Roger Lewis²

Received: 4 September 2024 / Revised: 29 October 2024 / Accepted: 30 October 2024
© The Author(s) 2025

Abstract

To mitigate and alleviate low wheel–rail adhesion, a train-borne system is utilised to deposit sand particles into the wheel–rail interface via a jet of compressed air in a process called rail-sanding. Britain Rail Safety and Standards Board introduced guidelines on the sand particles' shape, size, and uniformity which needs to be adhered to for rail-sanding. To further investigate these guidelines and help improve them, this research presents a parametric study on the particle characteristics that affect the rail-sanding process including density, size and size distribution, coefficient of uniformity, and shape, utilising a coupled computational fluid dynamics–discrete element method (CFD–DEM) model. The efficiency of rail-sanding is estimated for each case study and compared to the benchmark to optimise the sand characteristics for rail-sanding. It is concluded that particle size distribution (within the accepted range) has an insignificant effect on the efficiency while increasing particle size or the coefficient of uniformity decreases the efficiency. Particle shape is shown to highly affect the efficiency for flat, compact and elongated particles compared to the spherical shape. The current numerical model is capable of accurately predicting the trends in the efficiency compared to the actual values obtained from full-scale experiments.

Keywords Rail-sanding · CFD–DEM coupling · Numerical analysis · Particle characteristics

1 Introduction

The British railway industry annually spends around £345 million to mitigate the consequences of traction/adhesion¹ loss between the train's wheel and the rail. Low adhesion can occur due to the existence of a third body layer such as water, oil, and leaf on or bonded to the top of the rail. Adhesion loss during the train's acceleration and deceleration phases can result in train delays, safety risks, and in the worst-cases train collisions [1, 2].

To improve the railway transportation by increasing the wheel–rail adhesion, a train-borne system is utilised to deposit sand particles into the wheel–rail interface via a jet of compressed air to control the behaviour of the granular material. This process is called rail-sanding and is reliable in alleviating the effects of adhesion loss [1–4]. However,

in some circumstances, rail-sanding offers an efficiency of only < 20% which corresponds to > 80% of the deposited sand particles not being entrained into the wheel–rail interface thus playing no role in increasing the adhesion [5]. This means that the rail-sanding system can potentially be redesigned to optimise the efficiency of sand entrainment in the wheel–rail interface and thus reducing the risks of railway transportation as well as enhancing the sustainability of sand usage considering the limited resources of this natural material [1, 3, 6].

The rail-sanding process is often studied experimentally in controlled environments via twin-disc set-ups [3, 7, 8], and full-scale laboratory test rigs [5], or by performing field tests [9]. Although these tests are capable in offering accurate data, they can be expensive and inaccessible for the wider community. Another approach to study the rail-sanding process is using computational modelling which can provide accurate data in a less expensive and more accessible manner [10–12]. The dynamics of sand can be simulated using the discrete element method (DEM)

✉ Sadegh Nadimi
sadegh.nadimi-shahraki@ncl.ac.uk

¹ School of Engineering, Newcastle University, Newcastle upon Tyne NE1 7RU, UK

² Leonardo Centre for Tribology, Department of Mechanical Engineering, University of Sheffield, Sheffield S1 3JD, UK

¹ In the railway industry “adhesion” or “adhesion coefficient” is defined as the amount of traction present when the wheel–rail contact enters partial slip. In this paper, the terms are used interchangeably.

[10, 11] which can then be coupled to computational fluid dynamics (CFD) in either a two-way [13] or a one-way [14] approach to model the fluid-particle interactions. In our previous studies, first, DEM simulations of rail-sanding for various sander positions was validated by the experimental data presented by Lewis et al. [5]; and second, a one-way coupled CFD-DEM model was employed for a parametric study of the train characteristics that affect the efficiency of sand application (entrainment efficiency) such as the train velocity, the sand flow rate, and the nozzle geometry [14].

As a continuation of the previous research [14], the current paper presents a parametric study on the particle characteristics that affect the rail-sanding process. For this purpose, a coupled CFD-DEM model is utilised to simulate the rail-sanding process, the entrainment efficiency of sand particle is estimated for each case study and compared to the benchmark case and other cases to find the optimum sand for rail-sanding. The finding of this study can be used to refine the guidelines defining the characteristics of the sand particles used for rail-sanding. These guidelines are set by the organisation responsible for the safety of railway transport in each country. Here, the guidelines introduced by Great Britain Rail Safety and Standards Board (RSSB) in the second issue of GMRT2461 document are outlined as follows [15]:

- The sand shall, as far as possible, consist of rounded irregular shaped grains.
- The maximum proportion of grains of diameter <0.71 mm (22 British standard sieve mesh) shall be not more than 5% by weight.
- The maximum proportion of grains of diameter >2.8 mm (5 British standard sieve mesh) shall be not more than 5% by weight.
- The coefficient of uniformity (CoU) shall be less than 1.5. The CoU is defined as the ratio of the sand diameter at which 60% of the sand weight is finer to the corresponding value at 10% finer.

2 Methodology

2.1 Discrete element method

The discrete element method is used to simulate the behaviour of granular materials. This method employs the simple, but crucial, assumption of the particles being rigid discrete objects. Newton's and Euler's laws of translational and rotational motions [16] are then used to model the mechanical behaviour of the particles with the governing equations appearing as follows:

$$m_i \frac{dv_i}{dt} = \sum F_{Ci} + m_i g + F_{Di}, \quad (1)$$

$$\frac{d(I_i \cdot \omega_i)}{dt} = \sum M_{Ci}, \quad (2)$$

where m_i , I_i , v_i , and ω_i are the mass, the moment of inertia, the translational and the rotational velocities of the individual particle i , respectively; t is time and g is the gravitational acceleration; F_{Ci} and $M_{Ci} = R_i \times F_{Ci}$ are, respectively, the contact force and torque between each particle and its neighbouring particles and walls, R_i is the particle's radius [16], and F_{Di} is the drag force acting on the particle.

Particles interact with each other and the walls of the structures surrounding them. To model these interactions a suitable contact model should be used. In the present work, the elastic contact force, i.e. Hertz-Mindlin contact model, is chosen [16]. This contact model was shown to be accurate enough for the purposes of the current research [11].

2.2 Computational fluid dynamics

The continuity and Navier-Stokes equations [17] are used to model the dynamical behaviour of the fluid medium including both the jet of air that deposits the sand particles and the relatively stationary air surrounding all. These equations are presented as follows:

$$\nabla \cdot (U_f) = 0, \quad (3)$$

$$\rho_f \left(\frac{\partial U_f}{\partial t} + (U_f \cdot \nabla) U_f \right) = -\nabla P + \mu_f (\nabla^2 U_f), \quad (4)$$

where U_f , ρ_f , and μ_f are the fluid's velocity vector, density, and viscosity, respectively, and P is the pressure [17].

2.3 CFD-DEM coupling

The one-way coupling approach is chosen to link the DEM and CFD simulations together. This means that dynamics of the fluid affects the particle behaviour but not vice versa which is a reasonable assumption due to small sizes and low velocities of the particles compared to the whole system. This one-way coupled CFD-DEM modelling is performed by utilisation of the drag force acting on the sand particles, F_{Di} :

$$F_{Di} = \frac{1}{2} \rho_f C_D A |v_i - U_f| (v_i - U_f), \quad (5)$$

where C_D is the particles drag coefficient which is a function of the particle's Reynolds number (Re) and shape, and

A is the reference area of the particle. In most cases, the drag force dominates the majority of the particle dynamics [17, 18].

It was shown in our previous research that among the various models already presented in the literature for estimating the drag force, the model proposed by Ganser is versatile and results in a desirable accuracy in estimation of the drag force for various particle shapes [19]. So, the Ganser drag model [20] is utilised to estimate the particle's drag coefficient in the current research. The Ganser drag model uses the true sphericity of the particle, $\phi_w = A_{\text{sph}}/A_p$, defined by Wadell [21] as the ratio of surface area of the volume equivalent sphere (A_{sph}) to the particle surface area (A_p) to evaluate the drag coefficient of each particle:

$$C_D = \frac{24K_S}{Re} \left(1 + 0.1118 \left(\frac{ReK_N}{K_S} \right)^{0.6567} \right) + \left(\frac{0.4305K_N}{1 + \frac{3305}{ReK_N}} \right), \quad (6)$$

$$Re = \rho_f |v_i - U_f| \frac{d}{\mu_f}, \quad (7)$$

$$K_N = 10^{1.8148(-\log \phi_w)^{0.5743}}, \quad (8)$$

$$K_S = \frac{1}{3} + \left(\frac{2}{3} \sqrt{\phi_w} \right), \quad (9)$$

$$\phi_w = \frac{A_{\text{sph}}}{A_p}, \quad (10)$$

where K_S and K_N are Stoke's and Newton's drag correction factors, respectively, and d is the reference length of the particle.

The one-way CFD–DEM simulation is performed by first exporting the steady-state velocity field of the fluid from the CFD simulations and then importing it into the DEM model. After that, the chosen drag model is implemented in the DEM simulation to calculate the drag force on each discrete particle at each time step using the fluid velocity field and the dynamic and geometric properties of each particle.

2.4 Modelling the particle shape

The shape of natural sand grains used in rail-sanding application is rarely spherical. In classic DEM models, the shape of the particles is often simplified to spheres due to the already established contact detection algorithms and contact models for spherical particles. To represent particles' irregular shapes in DEM models, and still be able to utilise the established contact detection algorithms and contact models,

the complex geometries of the particles can be represented as clumps made of a number of either overlapping or non-overlapping spherical elements. This modelling approach can also retain the fine details of the particle's shape including local roundness, roughness, and concavities [22].

The number of the spherical elements used to represent the particle shape can significantly affect the accuracy and the cost of the computational simulation. To find the optimum number of spherical elements for the present study to accurately represent the particle shape without dramatically increasing the computational cost, irregular particles of different shapes are represented as multi-spheres clumps of ten different element numbers (one, two, five, ten, twenty, thirty, fifty, seventy, one-hundred, and two-hundred) generated by the Euclidean method utilising the CLUMP code [22]. The irregular particle shapes are classified in four shape categories of compact, flat, elongated, and bladed [23] based on the framework introduced by Zingg [24] and refined by Angelidakis et al. [23]. The multi-sphere representations of the irregular particles are then positioned facing the fluid flow at three orientations which correspond to the particle's minimum, median, and maximum area facing the flow resulting in the maximum, median, and minimum value of the drag coefficient, respectively. For each case, the drag coefficient is calculated through computational fluid dynamics by solving the continuity and Navier–Stokes equations for the fluid velocity field around the surface of the irregular particle and its multi-sphere representations. Figure 1 presents an example of representing the compact particle with various numbers of spherical elements at the orientation resulting in the maximum value of the drag coefficient for the actual shape. The multi-sphere representation of all the other particles at the three orientations is presented in the supplementary information document.

The drag coefficient of these multi-sphere clumps comprised of different numbers of spherical elements are compared to the drag coefficient of the actual shape at each of the three orientations of the minimum, median, and maximum area facing the flow. A summary of the results of the drag coefficient versus the number of spherical elements composing the multi-spheres is presented in Fig. 2.

For all cases, as the number of the spherical elements representing the irregular shape increases, the area facing the flow and the drag force also increases towards values closer to the values for the actual shape. Figure 2 shows that in most cases increasing the number of spherical elements of the clump representations results in a drag coefficient value closer to that of the actual shape. It is worth noting that representing the particle shape with its multi-sphere representation may create an artificial roughness on the surface of the particle which can influence the drag coefficient values.

For the three particle geometries of compact (Fig. 2a), flat (Fig. 2b), and elongated (Fig. 2c), the maximum difference

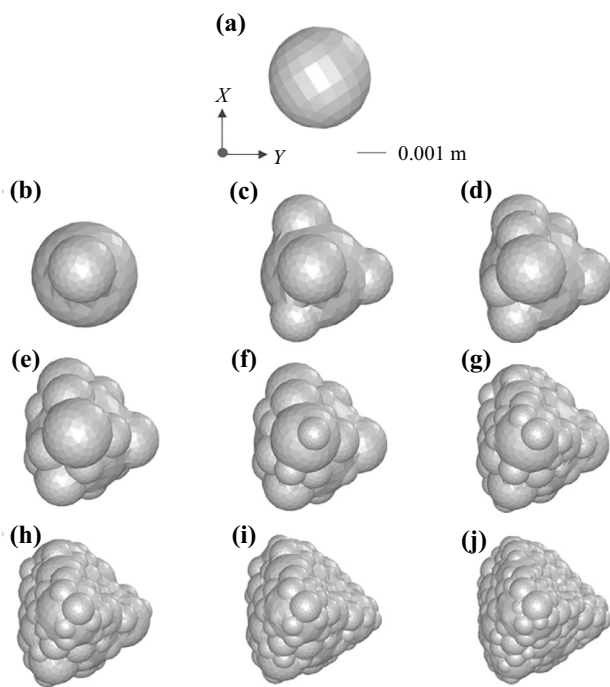


Fig. 1 Compact sand particle shape represented as a clump of a–j 1, 2, 5, 10, 20, 30, 50, 70, 100, and 200 spherical elements at the orientation resulting in the maximum value of the drag coefficient for the actual shape

between the values of the drag coefficient for the actual geometry and the multi-sphere representation using ten spherical elements is less than 18%. This can be considered acceptable for the purpose of the current study. So, particle shapes are represented as clumps of ten spherical elements in the CFD-DEM model to offer a compromise between the accuracy and the cost of the numerical modelling. The bladed particle geometry is not utilised in the current CFD-DEM model.

2.5 Numerical model set-up

In DEM, the model is established based on the geometry of the full-scale wheel–rail rig at the Leonardo Centre for Tribology—The University of Sheffield [5]. The set-up consists of a wheel with a P8 profile, a diameter of ~ 1016 mm, and an angular velocity of 0.098 Rad/s as well as a rail with a 60E1 profile, a width of ~ 70 mm, a length of roughly three wheel diameters, and a translational velocity of 0.05 m/s. The sander nozzle is cylindrical with a 150 mm length and a 25 mm diameter which is placed at a 20° angle relative to the rail [5, 11]. All the solid components are modelled as perfectly rigid. A ~ 0.3 kg of sand particles with a Young’s modulus of 70 GPa, and a Poisson’s ratio of 0.25 is loaded inside the hopper [2]. The coefficient of restitution (CoR) of the sand

particles which is defined in the DEM model to damp the sand particles’ bouncing of the wall is set to 0.5 [2, 25]. Figure 3 shows the details of geometry layout and dynamics of the DEM model.

The DEM modelling software EDEM (version 7.1.0) by Altair is used to perform the DEM simulations, with the time step set to 20% of the Rayleigh time step, which is calculated based on the size of the smallest particle. The application programming interface (API) in EDEM is used to implement the drag model into the DEM simulation. A total of 21 DEM simulations is reported here.

For the CFD model, the geometry is built according to the DEM model set-up, which comprises the sander pipes and nozzle connected to a rectangular cuboid. The boundary conditions are specified as known flow rate of 0.0034 kg/s at sander inlet, known ambient pressure at the two outlets, symmetry at the four sides of the rectangular cuboid, and no-slip (zero fluid velocity relative to the surface of the boundary due to fluid viscosity) on all the solid surfaces. The parts of the train wheel and rail which are located inside this cuboid are cut from the rectangular cuboid and act as moving walls with a rotational and a translational velocity of 0.098 rad/s and 0.05 m/s, respectively. Figure 4 shows details of the geometry layout and boundary conditions used for the CFD simulations.

The CFD simulation is carried out using ANSYS FLUENT (version 18.1) with the time step of 10^{-6} s and the convergence criteria set to 10^{-6} . The governing equations of the fluid motion are discretised using the finite volume method (FVM) which are then solved using the semi-implicit method for pressure-linked equations (SIMPLE).

Mesh dependency analysis is carried out to make certain of the independence of the simulation results from the resolution of the computational grid. This will ensure a desirable numerical accuracy, but minimises the cost and time associated with the computational simulations. In conclusion, a mesh resolution of a little more than 14,000,000 grid elements with quadratic shapes are used here. A total number of four CFD simulations for mesh dependency analysis have been performed.

The characteristics of the sand particles including density, size distribution, and shape are the parameters studied here. Figure 5 shows the particle size distribution graph used for the particle size investigation. Table 1 presents the values investigated for these three parameters. The five particle candidates (including the benchmark) used for the particle density study include the British rail-sand with a density of 2600 kg/m^3 as the benchmark along with recycled crushed glass, dolerite, coated alumina, and non-coated alumina with densities of 2500, 2900, 3700, and 3900 kg/m^3 , respectively.

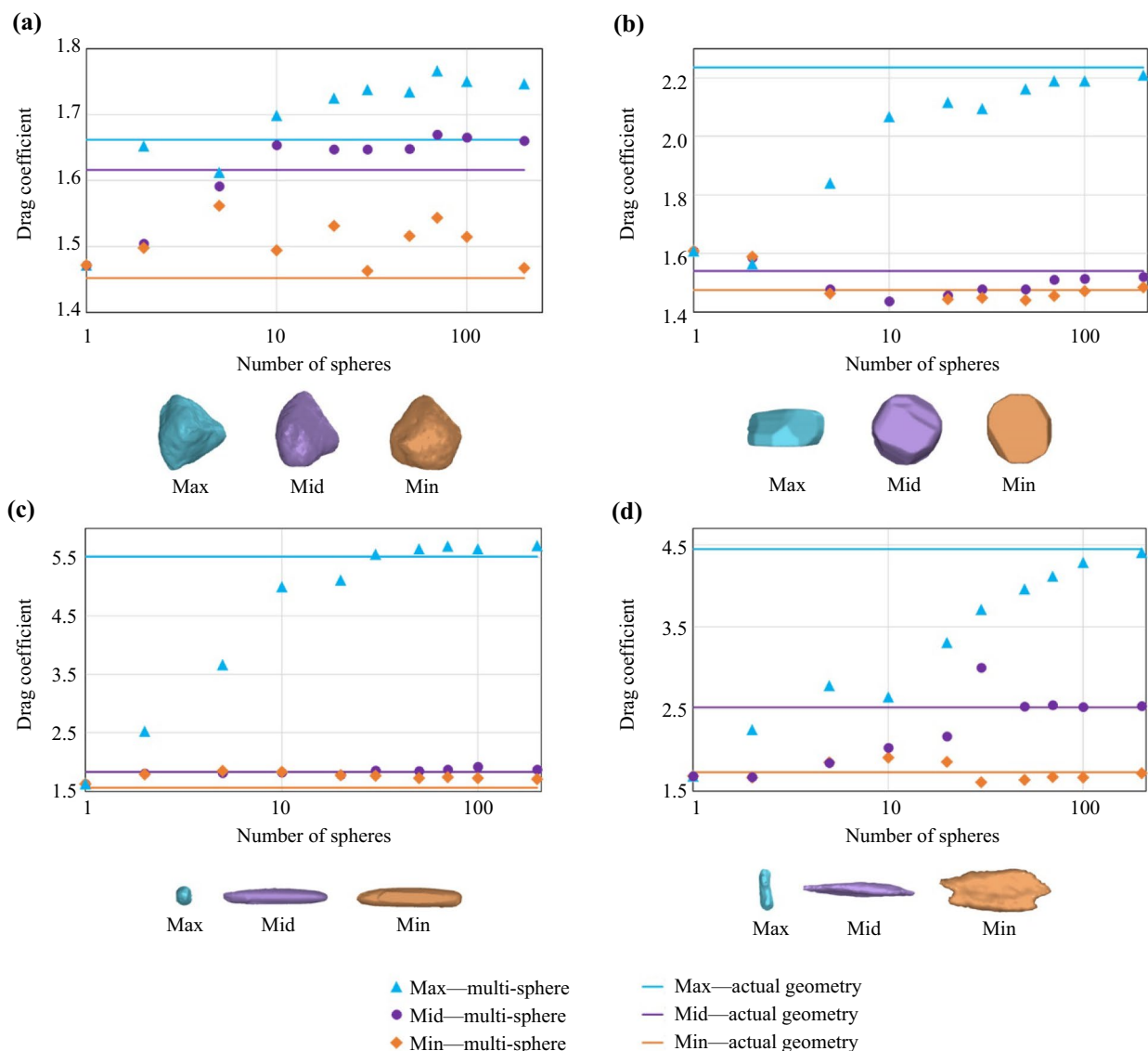


Fig. 2 Comparison of the drag coefficient values for the actual shape and the multi-sphere representations for the particle with **a** compact, **b** flat, **c** elongated, and **d** bladed irregular shape positioned at orienta-

tions which result in the minimum, median, and maximum values of the drag coefficient for the actual shape

2.6 Results and discussions

The entrainment efficiency reported in the results obtained through numerical modelling is calculated as the ratio of the number of particles reaching the wheel–rail interface and landing inside a virtual rectangular bin to the total number of particles which have landed on the railhead inside another larger virtual rectangular bin. In our previous study, it was shown that the entrainment efficiency of the sand particles is dependent on the size and location of these rectangular bins but for the same size bins at the same locations, the trends of entrainment efficiency are comparable [11]. Figure 6 presents a snapshot of the numerical simulation showing particle trajectories

coloured by their velocities as well as the two virtual rectangular bins used to estimate the entrainment efficiency. For the experimental investigations, the entrainment efficiency is measured by dividing the mass of the sand remaining on the rail’s surface after the wheel passed by the total mass of the sand used in the experiment [5]. It is worth mentioning that the numerical model simulates rail-sanding during the experiments performed in the laboratory [5] rather than during the actual train transport. Thus, the observations have some limitations, such as particles not being able to go through the wheel–rail interface due to the limited duration of the experiment, and the lack of longitudinal airflow.

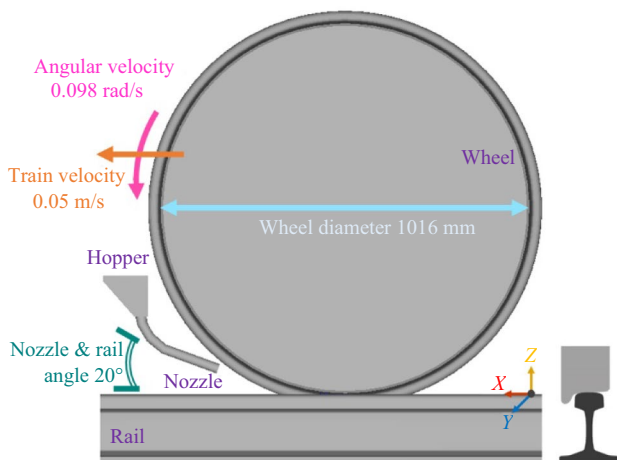


Fig. 3 Geometry layout for the DEM numerical model along with a frontal view of the 60E1 rail and P8 wheel profiles

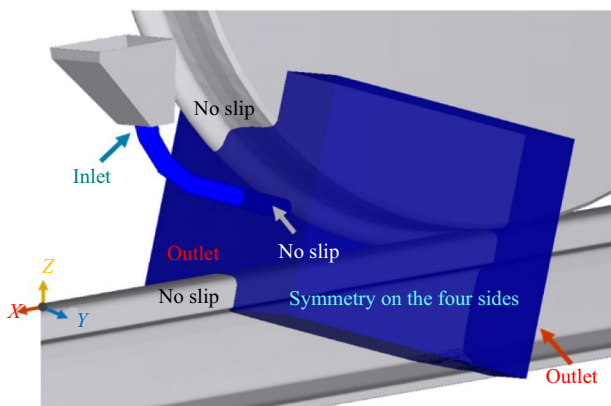


Fig. 4 Geometry layout and boundary conditions for the CFD model

2.7 Effects of particle density on the entrainment efficiency

Figure 7 shows the percentage change in entrainment efficiency of the rail-sanding for four sand density values compared to the benchmark case with a density of 2600 kg/m^3 for GB rail-sand. It can be seen that as the sand particle density affects the entrainment efficiency of the rail-sanding with a $\sim 50\%$ decrease when the density increases by $\sim 1000 \text{ kg/m}^3$, while a constant air flow rate of 0.0034 kg/s is applied. The decrease in the entrainment efficiency due to using particles with higher densities can be remedied by increasing the air flow rate as previously reported [14]. The significance of this conclusion is that if other particle candidates [26] with higher or lower densities compared to the GB rail-sand are utilised for rail-sanding, the entrainment efficiency of the particles can be recovered by tuning the air flow rate. This can justify using other alternatives instead of Great Britain

rail-sand due to the unsustainability of using sand or more favourable characteristics of other candidates [27].

2.8 Effects of particle size, size distribution, and coefficient of uniformity on the entrainment efficiency

The percentage change in entrainment efficiency of the rail-sanding compared to the benchmark case with a size distribution of 30% of 0.5 mm radius, 50% of 0.6 mm radius and 20% of 0.9 mm radius is shown in Fig. 8. Here, three distinct effects can be studied: the effect of particles' size shown in Fig. 8a, the effect of particles' size distribution presented in Fig. 8b, and effect of particles' coefficient of uniformity introduced in Fig. 8c. CoU is described as the ratio of the sieve size through which 60% by weight of the material passes to the sieve size that allows 10% by weight of the material to pass and the values are presented in Table 1.

Figure 8a shows that when the size distribution (the percentage representing the ratio of the coarse, the medium, and the fine sizes to the total amount of particles) remains the same, increasing the particle size lowers the entrainment efficiencies by $\sim 20\%$. This results in the introduction of maximum particle size suitable for rail-sanding. The effect of particle size distribution for particles of the similar size is negligible on the entrainment efficiency as can be seen in Fig. 8b. Figure 8c illustrates that if CoU is higher than 2.5, the entrainment efficiency may decrease by $\sim 20\%$ which is in line with the guidelines presented in [15] stating "The uniformity coefficient shall be less than 1.5".

2.9 Effects of particle shape on the entrainment efficiency

Figure 9 shows the three particle shapes of compact (Fig. 9a), flat (Fig. 9b), and elongated (Fig. 9c) represented as multi-spheres of ten spherical elements in the DEM simulation. The elongated particle is then truncated by two, four, six, and eight spherical elements symmetrically from both ends to form particles presented in Fig. 9 c-1 to c-4. Particles with inherent elongated shapes can be produced such as the many RCG particles presented in [26, 27]. Bladed particles are not considered when studying the effect of shape as they are rarely encountered in natural sand and alumina particles [26].

The percentage change in entrainment efficiency of the rail-sanding process for the three sand shapes of compact, flat, and elongated as well as the truncated forms of the elongated particle by two, four, six, and eight spherical elements compared to the benchmark case with spherical sand is presented in Fig. 10. It can be concluded that among the three shape categories of compact, flat, and elongated particles of the same size, the flat particle

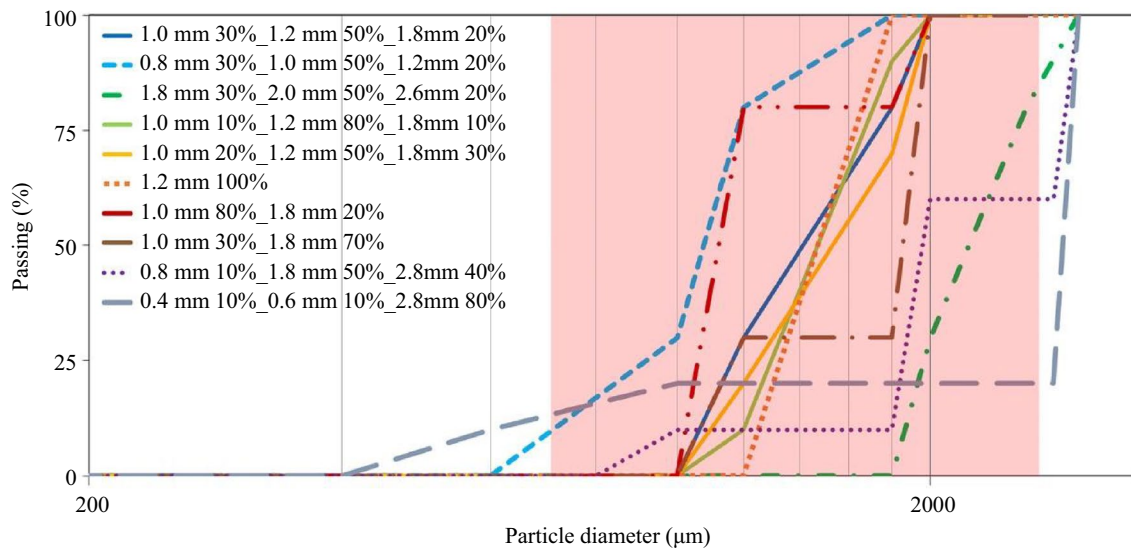


Fig. 5 Particle size distribution graph used for the particle size investigation; the red area shows the size range currently accepted by GMRT 2461[15]

Table 1 Parameters investigated for the parametric study

Parametric study	Particle Density (kg/m ³)	Particle diameter (mm) (size distribution)	Coefficient of uniformity	Particle shape
Benchmark	2600	1.0 (30%), 1.2 (50%), 1.8 (20%)	1.5	Spherical
Particle density study	2500	1.0 (30%), 1.2 (50%), 1.8 (20%)	1.5	Spherical
	2900	1.0 (30%), 1.2 (50%), 1.8 (20%)	1.5	Spherical
	3700	1.0 (30%), 1.2 (50%), 1.8 (20%)	1.5	Spherical
	3900	1.0 (30%), 1.2 (50%), 1.8 (20%)	1.5	Spherical
	Particle radius and size distribution study	2600	0.8 (30%), 1.0 (50%), 1.2 (20%)	1.6
2600		1.8 (30%), 2.0 (50%), 2.6 (20%)	1.3	Spherical
2600		1.0 (10%), 1.2 (80%), 1.8 (10%)	1.3	Spherical
2600		1.0 (20%), 1.2 (50%), 1.8 (30%)	1.5	Spherical
2600		1.2 (100%)	1.0	Spherical
2600		1.0 (80%), 1.8 (20%)	1.2	Spherical
2600		1.0 (30%), 1.8 (70%)	1.8	Spherical
2600		0.8 (10%), 1.8 (50%), 2.8 (40%)	2.0	Spherical
2600		0.4 (10%), 0.6 (10%), 2.8 (80%)	5.0	Spherical
Particle shape study	2600	1.2 (100%)	1.0	Compact 10 elements
	2600	1.2 (100%)	1.0	Flat 10 elements
	2600	1.2 (100%)	1.0	Elongated 10 elements
	2600	1.2 (100%)	1.0	Truncated 8 elements
	2600	1.2 (100%)	1.0	Truncated 6 elements
	2600	1.2 (100%)	1.0	Truncated 4 elements
	2600	1.2 (100%)	1.0	Truncated 2 elements

results in the maximum entrainment efficiency with more than ~50% increase compared to the benchmark case. This is followed by the elongated and compact particles with more than ~30% and ~15% increase in the entrainment efficiency, respectively.

Comparing the elongated particle to its truncated forms, it can be seen that the effect of shortening the particles by two elements on the entrainment efficiency can be considered negligible, while the further truncation of the particle shape reduces the entrainment efficiency. One interesting

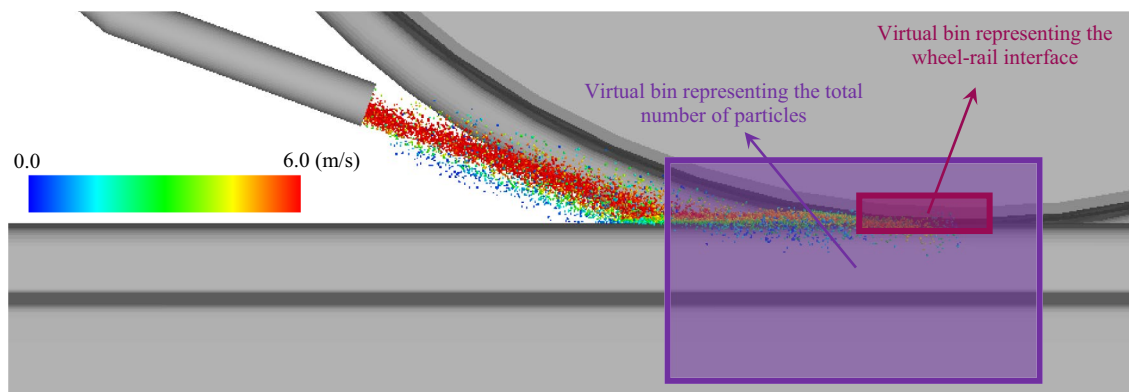


Fig. 6 A snapshot of the numerical simulation of the rail-sanding showing GB rail-sand particle trajectories at a set timestep coloured by their velocities as well as the two virtual rectangular bins used to estimate the entrainment efficiency

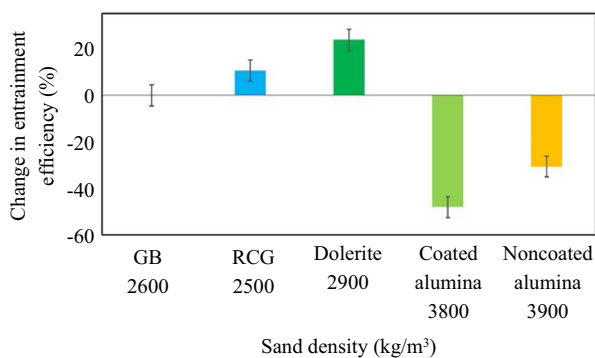


Fig. 7 Percentage change in entrainment efficiency of the rail-sanding for four values of particle density compared to the benchmark case of 2600 kg/m³ density for GB rail-sand

observation is the considerable decrease in the entrainment efficiency for the case c-3 which can be explained by the overall shape of the truncated forms of the elongated particles. In Fig. 9, it can be seen that the multi-spheres named c-1, c-2, and c-4 appear to be relatively straight while the multi-sphere named c-3 is slightly curved into an S-shaped structure. The interaction of these S-shaped particles with the air medium around them is different compared to the straight particles resulting in the curved S-shaped particles to deviate more from the relatively linear trajectories usually followed by straight particles.

2.10 A blind prediction with full-scale experiments

The simulations are blindly performed with limited information on the operational conditions of the full-scale experiments. The optimum case of 20° angle between the nozzle and the rail from [11] is used as the benchmark. Full-scale experiments are undertaken on a full-scale rig (FSR), a schematic of which is presented in Fig. 11a. The FSR is the same rig as used by Lewis et al. [5] for their study and utilises a

very similar sanding apparatus, with the same compressor, hopper, valve, and hose and only having minor differences elsewhere (i.e. cameras used). Figure 11b shows the actual photograph of the full-scale rig.

The FSR is made of a train wheel ①, supported by a frame ②. The wheel is on top of a ~1 m piece of rail ③, which rests upon a bed ④ with low friction Polytetrafluoroethylene (PTFE) strips to allow for smooth longitudinal motion of the rail; the motion of the bed and rail is controlled by an actuator ⑤. A realistic wheel load can be applied with another actuator ⑥. The sanding apparatus is made up of a hopper and hose ⑦, with a stream of compressed air (supplied by an 8 bar, Bambi MD 150/500 compressor ⑧) picking up particles in the hopper and depositing them from the hose onto the rail. The two cameras ⑨ are installed to record the process.

The position of the hose is kept the same throughout (10° to the rail, 300 mm from the contact patch, and 20 mm above the rail) and the compressor pressure is adjusted for each material to deliver 2 kg/min. In order to enable particle entrainment for the alumina particles, a higher sanding rate is applied due to their higher densities. In all case studies, the rail moves in the longitudinal direction with a velocity of 0.1 m/s. The sanding system is activated during one wheel pass over 300 mm of rail, and crushed material is gathered from 150 mm of railhead after each test. In these experiments, and the entrainment efficiency of the rail-sanding process is defined as the ratio of the average mass of crushed sand remaining on 150 mm of the railhead after the wheel has passed to the ideal mass of sand which should theoretically remain on 150 mm of the railhead. Applying sand with a flow rate of 2 kg/min from the sander on 150 mm of the rail moving at 0.1 m/s results in the ideal mass of 50 g sand which should remain on the railhead to produce a 100% entrainment efficiency. Table 2 presents the values investigated for the full-scale experiments. It is worth mentioning that the inconsistencies in Table 2 are mostly due to the amount of material which is available.

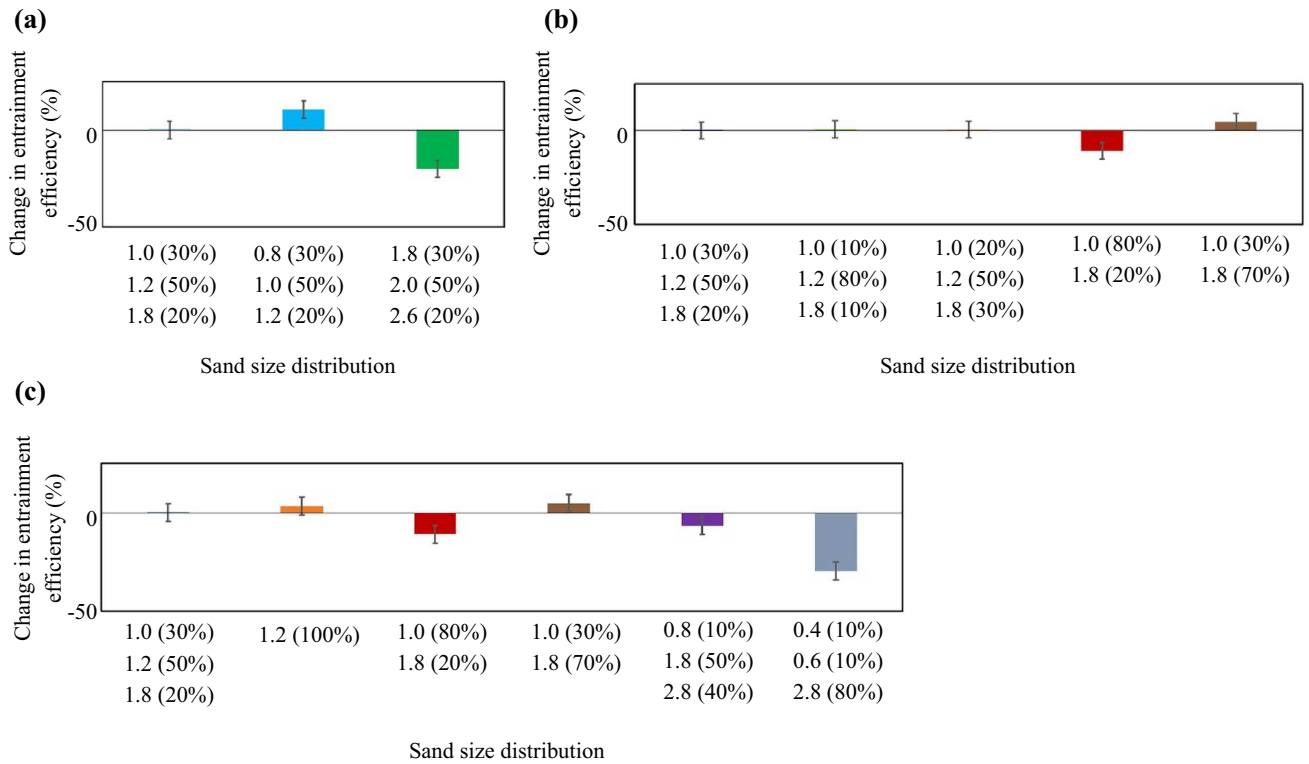


Fig. 8 Percentage change in entrainment efficiency of the rail-sanding showing the effects of **a** particle size with constant size distribution, **b** particle size distribution, and **c** coefficient of uniformity of particles

compared to the benchmark case with a size distribution of 30% of 0.5 mm radius, 50% of 0.6 mm radius and 20% of 0.9-mm radius

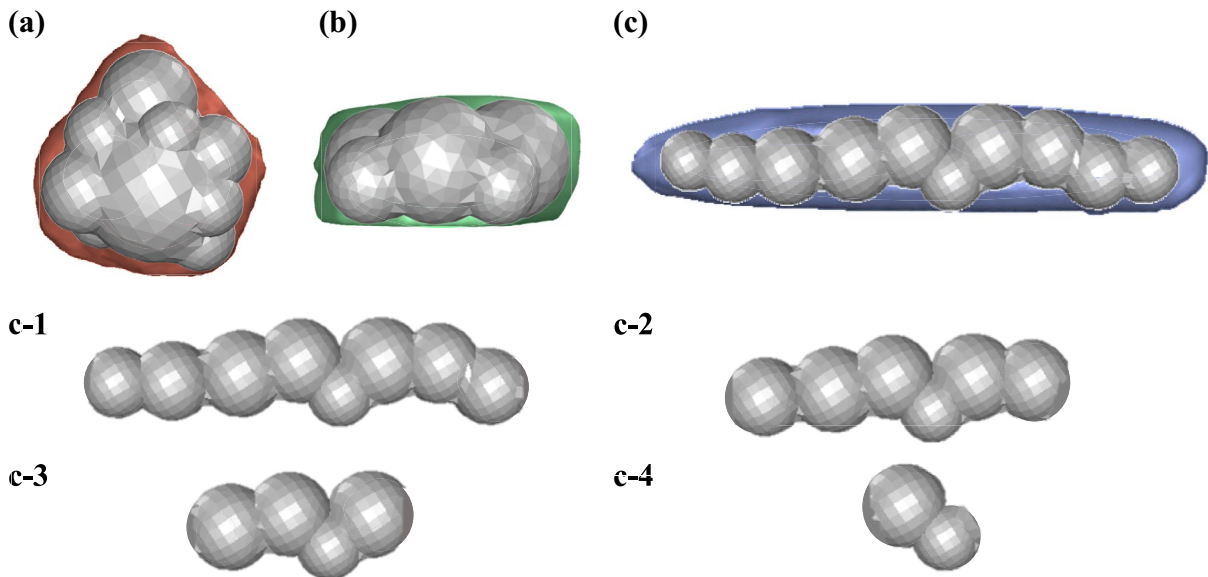


Fig. 9 Shapes and multi-sphere representations of **a** compact, **b** flat, and **c** elongated particles; represented with ten spherical elements; and the elongated particle truncated by two, four, six, and eight, spherical elements (c-1 to c-4) symmetrically from both ends

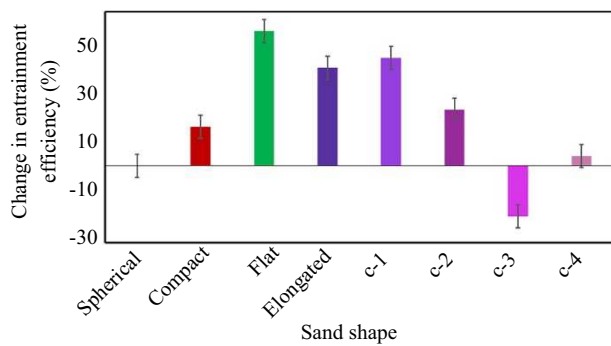


Fig. 10 Percentage change in entrainment efficiency of the rail-sanding for three particle shapes compared to the benchmark case of spherical sand shape

The entrainment efficiency of the rail-sanding for GB rail-sand and four rail-sand alternatives, namely recycled crushed glass (RCG) of three different sizes of 2 mm, 1.18 mm, and 0.6 mm [27], coated alumina, non-coated alumina, and dolerite [26] obtained through numerical simulations is blindly compared to the data obtained from full-scale experiments, and the values and trends are shown in Fig. 12. As previously explained, to calculate the entrainment efficiency of the sanding experiments, the average amount or

sand remaining on the rail in grams (from Table 2) is divided by the ideal amount of 50 g.

It can be seen that the numerical simulation is able to accurately predict the trends in the entrainment efficiency with a maximum of $\leq 5\%$ difference in the actual values which corresponds to a few milligrams of the material. The full-scale experiments resulting in lower values of particle entrainment efficiency compared to the numerical simulation is expected as even controlled environments can introduce undesirable effects to the experimental data compared to the ideal setting of numerical simulations.

Comparing the entrainment efficiency of the three sizes of RCG particles presented in Fig. 12, it can be seen that the maximum entrainment efficiency occurs for the 1.18 mm particles and increasing the particle size to 2 mm or decreasing it to 0.6 mm lowers the entrainment efficiency. This is in alignment with the guidelines presented in [15] indicating the optimum particle size distribution which is $0.71 \text{ mm} \leq \text{particle diameter} \leq 2.8 \text{ mm}$.

In Fig. 12, a noticeable disparity between the values of entrainment efficiency obtained from numerical modelling using coated Alumina and non-coated Alumina particles can be seen. One reason for this disparity can be that in the numerical modelling the only difference between coated alumina and non-coated alumina particles is their

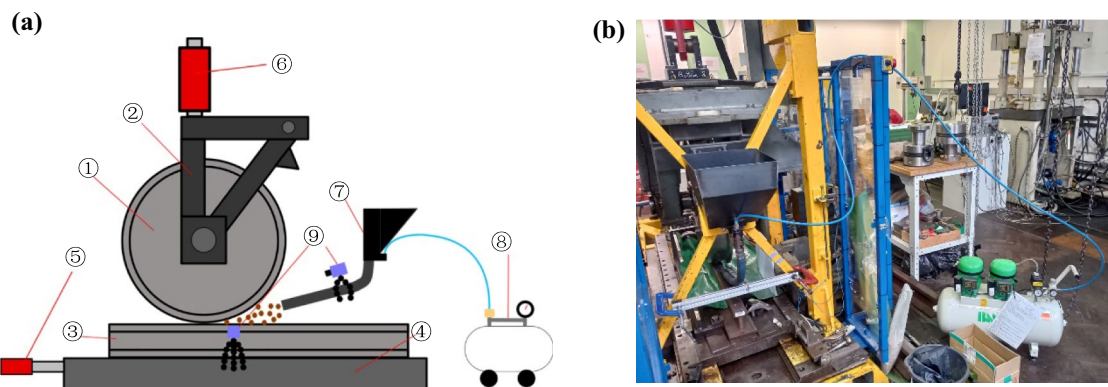


Fig. 11 **a** Schematic of full-scale rig apparatus as used for this study; **b** actual photo of the full-scale rig

Table 2 Values investigated for the full-scale experiments

Sand type	Starting pressure (bar)	Time (s)	Output (kg/min)	Average amount of sand remaining on rail (g)
British rail-sand	7	15	2.0	4.801
Recycled crushed glass 2 mm	7.5	15	1.9	1.627
Recycled crushed glass 1.18 mm	8	10	1.9	3.777
Recycled crushed glass 0.6 mm	8	5	2.0	2.116
Coated alumina	8	15	2.2	2.157
Non-coated alumina	7.5	15	2.0	0.757
Dolerite	7.5	3	2.0	4.484

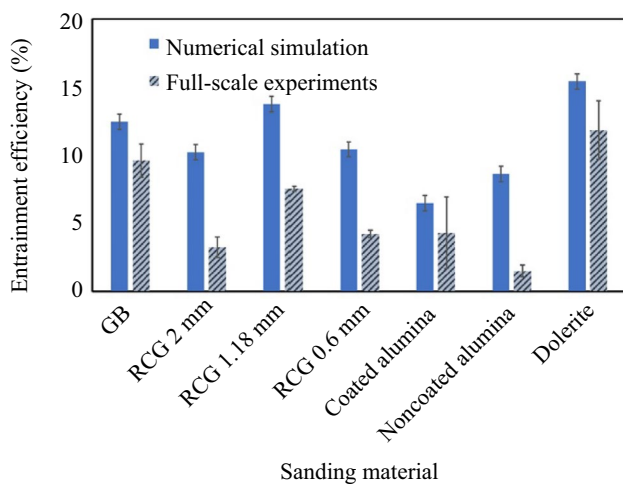


Fig. 12 Entrainment efficiency of the rail-sanding for GB rail-sand and four rail-sand alternatives compared to the data obtained from full-scale test rig experiments

corresponding densities, while in reality (as well as the experiments) coated alumina particle are treated with a coating that can affect their surface properties which in turn may change the entrainment efficiency of the experiments compared to the numerical model.

3 Conclusions

In this research numerical simulations using CFD–DEM coupling were performed to model the rail-sanding process and present a parametric study on the sand particle characteristics by comparing particle entrainment efficiency obtained from the CFD–DEM model for various case studies to the benchmark case. It was shown that when the particle density increases by $\sim 1000 \text{ kg/m}^3$, the entrainment efficiency of rail-sanding is decreases by $\sim 50\%$ which can be rectified by increasing the air flow rate inside the sander. This can justify utilising other particle alternatives due to the unsustainability of using sand or more favourable characteristics of other candidates. The effects of particle size, size distribution, and coefficient of uniformity were shown to be as follows: increasing the particle size reduces the entrainment efficiencies by $\sim 20\%$, particle size distribution (within the accepted range of the standard) has negligible effect on the entrainment efficiency, and increasing the coefficient of uniformity higher than 2.5 decreases the entrainment efficiency by a maximum of $\sim 20\%$. Particle shape highly affects the entrainment efficiency with more than $\sim 50\%$, $\sim 30\%$, and $\sim 15\%$ increase for flat, elongated, and compact particles compared to the spherical shape, respectively. A blind comparison of the numerical simulation results to full-scale experiments for GB rail-sand and four rail-sand alternatives has also been

performed. The numerical simulation was shown to be capable in accurately predicting the trends of the entrainment efficiency with only a $\leq 5\%$ difference compared to the actual values obtained from full-scale tests.

Acknowledgements This work was funded by the UK Engineering and Physical Sciences Research Council (EPSRC) grant No. EP/V053655/1 RAILSANDING—Modelling Particle Behaviour in the Wheel–Rail Interface. The authors would like to acknowledge the partnership with, and the support received from Altair, and Engineering and Physical Sciences Research Council, EP/ V053655/1, Sadegh Nadimi.

Open Access This article is licensed under a Creative Commons Attribution 4.0 International License, which permits use, sharing, adaptation, distribution and reproduction in any medium or format, as long as you give appropriate credit to the original author(s) and the source, provide a link to the Creative Commons licence, and indicate if changes were made. The images or other third party material in this article are included in the article's Creative Commons licence, unless indicated otherwise in a credit line to the material. If material is not included in the article's Creative Commons licence and your intended use is not permitted by statutory regulation or exceeds the permitted use, you will need to obtain permission directly from the copyright holder. To view a copy of this licence, visit <http://creativecommons.org/licenses/by/4.0/>.

References

1. Skipper WA, Chalisey A, Lewis R (2018) A review of railway sanding system research: adhesion restoration and leaf layer removal. *Tribol-Mater, Surf & Interfaces* 12(4):237–251
2. Skipper WA, Nadimi S, Chalisey A et al (2019) Particle characterisation of rail sands for understanding tribological behaviour. *Wear* 432:202960
3. Arias-Cuevas O, Li Z, Lewis R (2011) A laboratory investigation on the influence of the particle size and slip during sanding on the adhesion and wear in the wheel–rail contact. *Wear* 271(1–2):14–24
4. Cooper PR (1972) An investigation into the relationship between the particle size and the frictional performance of sand. IM-ADH-011, British Rail Research
5. Lewis S, Riley S, Fletcher D et al (2018) Optimisation of a railway sanding system for optimal grain entrainment into the wheel–rail contact. *Proc Inst Mech Eng Part F J Rail Rapid Transit* 232(1):43–62
6. Skipper W, Chalisey A (2020) Lewis R (2020) A review of railway sanding system research: Wheel/rail isolation, damage, and particle application. *Proc Inst Mech Eng Part F J Rail Rapid Transit* 234(6):567–583
7. Lewis R, Dwyer-Joyce R (2006) Wear at the wheel/rail interface when sanding is used to increase adhesion. *Proc Inst Mech Eng Part F J Rail Rapid Transit* 220(1):29–41
8. Wang C, Shi L, Ding H et al (2021) Adhesion and damage characteristics of wheel/rail using different mineral particles as adhesion enhancers. *Wear* 477:203796
9. Arias-Cuevas O, Li Z (2011) Field investigations into the performance of magnetic track brakes of an electrical multiple unit against slippery tracks. Part 1: Adhesion improvement. *Proc Inst Mech Eng Part F J Rail Rapid Transit* 225(6):613–636.
10. Descartes S, Renouf M, Fillot N et al (2008) A new mechanical–electrical approach to the wheel–rail contact. *Wear* 265(9–10):1408–1416

11. Maramizonouz S, Nadimi S, Skipper W et al (2023) Numerical modelling of particle entrainment in the wheel–rail interface. *Comput Part Mech* 10:2009–2019
12. Duan F (2015) Numerical tribology of the wheel–rail contact: Application to corrugation defect, Dissertation, INSA de Lyon
13. Gautam A, Green S (2020) Computational fluid dynamics discrete element method simulation of locomotive sanders. *Proc Inst Mech Eng Part F J Rail Rapid Transit* 235(1):12–21
14. Maramizonouz S, Nadimi S, Lewis R (2024) CFD-DEM modelling of particle entrainment in wheel–rail interface: a parametric study on train characteristics. *Acta Mech* 235:6077–6087
15. Rail Safety and Standards Board (2018) Sanding equipment (issue 3), GMRT2461
16. Thornton C (2015) Granular dynamics, contact mechanics and particle system simulations: A DEM study. Springer, Cham
17. White FM (1979) Fluid mechanics. McGraw-Hill, New York
18. Crowe CT, Michaelides EE (2006) Multiphase flow handbook. CRC Press, Boca Raton
19. Maramizonouz S, Nadimi S (2022) Drag force acting on ellipsoidal particles with different shape characteristics. *Powder Technol* 412:117964
20. Ganser GH (1993) A rational approach to drag prediction of spherical and nonspherical particles,. *Powder Technol* 77(2):143–152
21. Wadell H (1932) Volume, shape, and roundness of rock particles,. *J Geol* 40(5):443–451
22. Angelidakis V, Nadimi S, Otsubo M et al (2021) CLUMP: a code library to generate universal multi-sphere particles. *SoftwareX* 15:100735
23. Angelidakis V, Nadimi S, Utili S (2022) Elongation, flatness and compactness indices to characterise particle form. *Powder Technol* 396:689–695
24. Zingg T (1935) Beitrag zur Schotteranalyse. Dissertation, ETH Zurich
25. Tsuji Y, Tanaka T, Ishida T (1992) Lagrangian numerical simulation of plug flow of cohesionless particles in a horizontal pipe. *Powder Technol* 71(3):239–250
26. Maramizonouz S, Nadimi S, Skipper W et al (2023) Characterisation of physical and mechanical properties of seven particulate materials proposed as traction enhancers. *Sci Data* 10(1):400
27. Maramizonouz S, Nadimi S, Skipper W et al (2023) Characterisation and tribological testing of recycled crushed glass as an alternative rail sand. *Proc Inst Mech Eng Part F J Rail Rapid Transit* 237(10):1353–1358